Voxel-Scale Conversion Mapping Informs Intrinsic Resolution in Stereolithographic Additive Manufacturing

Tobin E. Brown, Veruska Malavé, Callie I. Higgins, Anthony P. Kotula, Benjamin W. Caplins, Edward J. Garboczi, and Jason P. Killgore*

Cite This: https://dx.doi.org/10.1021/acsapm.0c01090

Read Online

ACCESS | 📊 Metrics & More | 📄 Article Recommendations | 🆂ᴵ Supporting Information

ABSTRACT: In high-resolution stereolithography, printed parts deviate significantly from the projected photomask because of the reaction complexity on the voxel scale. To better understand the reaction process, we have developed a technique to measure local photopolymerization rates using a nanocylinder-tipped atomic force microscope cantilever. The drag force experienced during cantilever oscillations can be correlated to the viscosity and extent of reaction. Fluid dynamics simulations show micrometer-scale measurement localization, and the resonance-based measurement allows submillisecond temporal resolution. In a thiol—ene resin exposed to patterned light, oligomer diffusion length scales are significant compared to the size of printed structures. Consequently, part resolution is dictated by the competition between polymerization and diffusion. Because of the radical polymerization mechanism, increasing the light intensity at a constant dose decreases the local conversion, even though the diffusion length decreases. In the case of printed test structures with features matching the measured diffusion lengths, increased light intensity causes increased geometric aberration from the projected mask. Overall, the results indicate a need for enhanced control over polymerization and diffusion to obtain dimensionally accurate and mechanically homogeneous parts.

KEYWORDS: *additive manufacturing, photopolymerization, scanning probe microscopy, rheology, computational fluid dynamics*
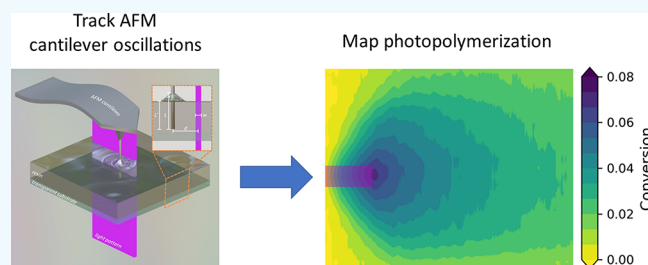
■ INTRODUCTION

Stereolithography (SLA) is an additive manufacturing technique where a liquid photopolymer resin is solidified by selective exposure to light in a layer-by-layer approach to generate a three-dimensional object.[1] Compared to the thermoplastic materials used in fused deposition modeling, the thermoset polymers resulting from SLA are solvent- and heat-resistant,[2] and they can confer a wide range of mechanical properties and high print resolution to the final part.[3] This makes stereolithography an attractive option for demanding applications from aerospace to tissue engineering. With stereolithography trending toward a mainstream manufacturing technology, current research endeavors focus on predicting and controlling the final mechanical properties and resolution of the printed part. However, these parts exhibit intrinsic mechanical heterogeneity and poor dimensional accuracy that is not explained by simple critical energy dose models[4] that pervade the field. Moreover, resolution requirements for new applications in metamaterials and bioprinting (e.g., human cell scale <10 μm) push the limits of what is currently achievable in scalable single-photon processes.[5] The ability to print parts with the highest resolution and most precise spatial control of mechanical properties hinges on an increased understanding of the underlying photopolymerization processes involved.[6]

As a resin reacts from a liquid to a solid, larger polymeric species form, contributing to an increase in viscosity and eventually leading to gelation, the formation of a percolating three-dimensional network that begins to define the final shape of the additively manufactured part.[7] We recently developed a new scanning probe technique using an atomic force microscope (AFM) cantilever vibrational resonance to track photopolymerization with nanometer spatial resolution and microsecond temporal resolution.[8] Termed sample-coupled resonance photorheology (SCRPR), the effect of cure on the resonance characteristics of an oscillating cantilever can be related to the increased stiffness and reduced damping caused by cross-linking.[8] In the previous work, the primary test sample was a dual cure polymer network that underwent a rubber-to-glass transition upon localized UV exposure. Those measurements were made in a more traditional nanomechanics configuration with the tip indenting the photopolymer, thus allowing conventional AFM probes to be used. In the current
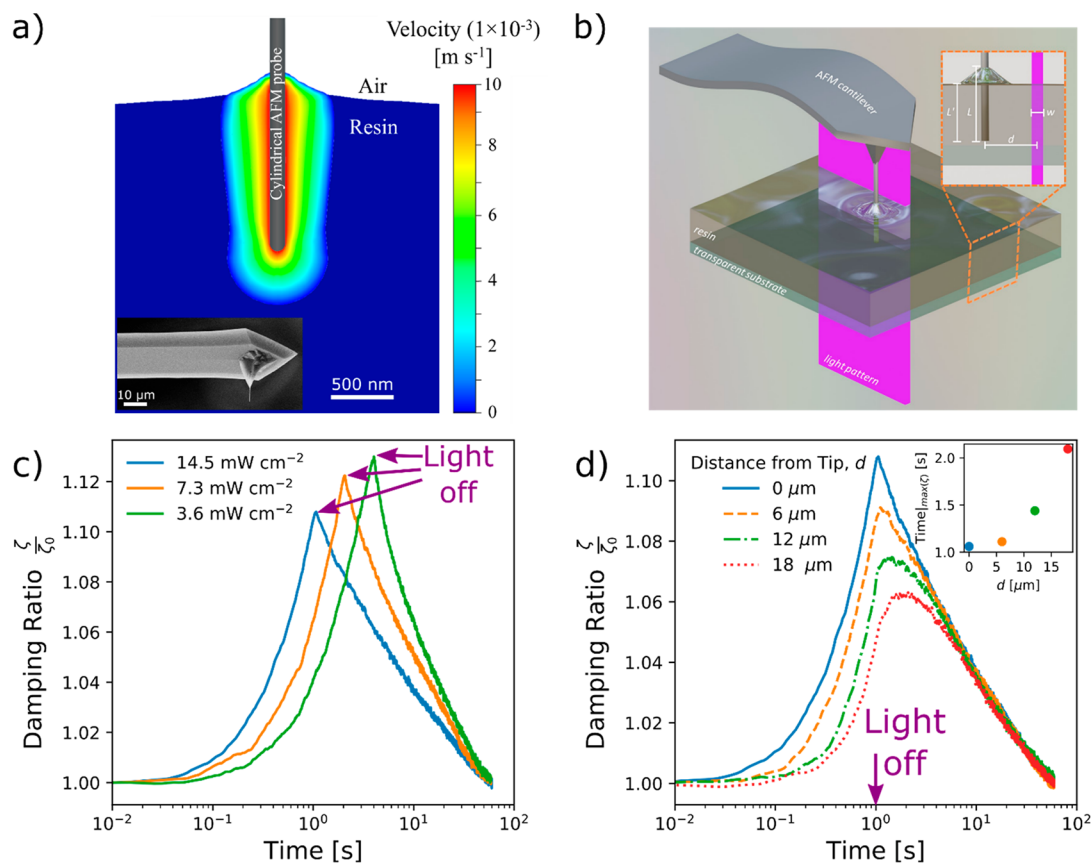
A

Figure 1. Nanocylindrical AFM probes allow for localized measurement of liquid drag forces and rheological properties. (a) Velocity field determined by CFD shows the motion of the proximal fluid induced by probe oscillations. The velocity gradient is a function of position along the probe. Inset: scanning electron micrograph of an AFM probe with a nanocylinder extending from the tip. (b) A hybrid AFM+SLA instrument allows local SCRPR measurements relative to a patterned light source that illuminates the resin from below. (c) Adjusting light intensity alters the reactions rate for exposures with an equal total dose of 14.5 mJ cm^{-2}. The increase in viscosity is reversible below the gel point of the resin. After 1 s (blue), 2 s (orange), or 4 s (green) of light exposure, the light source is shuttered to allow the polymerized species to diffuse away from the focal volume, resulting in a decrease in damping. This allows subsequent light exposures to be performed in the same location after allowing sufficient time (1 min) for the reaction volume to equilibrate. (d) Translating the light source relative to the probe allows for the spatial and temporal mapping of the generation and diffusion of polymeric species. Increased damping is observed at earlier time points when the exposure region coincides with the probe. Inset: as d increases, the maximum damping occurs later after the light is shuttered due to the time required for the polymerized species to diffuse to the sensing region.

work, we present a method to quantify conversion and diffusion in the liquid resin through changes in its viscosity during SLA photopolymerization. We build from the work of Cohn and co-workers, who measured fluid viscosity using a nanocylinder suspended from an AFM cantilever.[9] By using a nanocylindrical probe and relating monomer conversion to viscosity with rheo-Raman spectroscopy, we can use the damping of an oscillating cantilever to directly measure the spatiotemporal evolution of polymeric species throughout polymerization. We investigate the effects of light intensity and photopattern size on the reaction conversion profile and find that the radical polymerization mechanism limits the usefulness of increased light intensity to enhance feature resolution by decreasing conversion at a constant dose. We also detect polymeric species diffusion tens of micrometers away from illuminated pixels within seconds, which affects the final shape of printed test structures. Finally, the significant effect of diffusion is confirmed by nanoscale characterization of enclosed solid ring structures which exhibit asymmetry between enclosed and open walls.

RESULTS AND DISCUSSION

To determine the suitability of SCRPR measurements to map the SLA voxel-scale reaction profile, it is necessary to establish the spatial resolution of the method. Previous SCRPR measurements were performed with pyramid-shaped tips typical of AFM probes, which are poorly suited to localized viscosity measurements of liquids due to their taper. Specifically, as the sharp tip is inserted into the test fluid, a meniscus forms and rapidly extends upward on the tip, creating an ever larger solid–liquid contact line and delocalizing the sensing ability of the probe. In contrast, cylindrical AFM probes have a constant diameter and thus maintain a constant contact line and capillary force as the probe is lowered into the fluid (Figure S1). Assuming a Newtonian liquid, the damping of such an oscillating cantilever is a function of the inserted cylinder length and liquid viscosity.[9] To model the hydrodynamics in the experimental geometry, we employed computational fluid dynamics (CFD) analysis, which allows us to predict the damping force encountered by the oscillating cylinder and to examine the velocity profiles within the proximal liquid. These velocity profiles indicate the amount of resin perturbed by the probe's motion and therefore govern the

resolution of the measurement. An axisymmetric CFD model was constructed by using a finite volume approach in a commercial CFD package (Fluent, Ansys). In the model, a 60 nm radius cylinder with a hemispherical end-cap is inserted into a Newtonian fluid and oscillated with an amplitude of 5 nm and frequency of either 50 or 300 kHz. For simulation, three fluids with viscosities η of 202, 600, and 4700 mPa·s, spanning a range typical for photopolymer resins (Table S1), were used. A premodel step was included to allow formation and equilibration of the meniscus, resulting in a 220 nm meniscus rise and a 13.5 nN capillary force, in reasonable agreement with experiment (≈250 nm and 15.5 nN, Figure S1).

The CFD model results are shown as a velocity field in Figure 1a (the full extent of the experiment with the boundaries is shown in Figure S2). The fluid velocity decays rapidly from the probe's velocity at the nonslip surface to negligible values within several hundred nanometers. The total drag force imposed on the probe can also be calculated and is presented for each fluid and oscillation frequency in Table S2 at two insertion lengths (820 and 1420 nm). The viscous drag on cylindrical bodies moving within fluids has been studied extensively, and several relationships exist to calculate such forces. A relationship proposed by Broersma[10,11] (see the Methods section) describes the drag force as a function of cylinder geometry, velocity, and fluid viscosity. Comparison of the drag forces from our simulation with those calculated with Broersma's method shows good agreement over the range of parameters tested (Table S2). Interestingly, the velocity profiles indicate that the sensing resolution is likely better than 1 μm, representing an improvement over the estimate for an infinite cylinder provided by Ondárçuhu and co-workers.[12] This may be explained in part by examination of the effect of insertion length on the velocity field (Figure S2). As the cylinder is inserted further into the fluid, the velocity gradient diminishes, and more fluid is perturbed. This is likely due to the constriction of the velocity field near the tip relative to the body of the probe, as seen in Figure 1a. As the insertion length increases, the relative contribution from the cylinder tip and liquid–air interface lessens, and the viscous layer thickness increases. These results indicate that such geometric effects, which are not captured in the Stokes solution (eq S2), may alter the fluid flow near the cylinder and ultimately enhance the spatial resolution beyond the Stokes prediction.

We next turned to AFM experiments to corroborate these findings using test fluids (N100, N350, and S2000, Cannon Instrument Co.) with specified viscosities that matched those simulated above. To rapidly evaluate the cantilever responses in the known viscosity fluids, we employed dual AC resonance tracking (DART)[13] force vs distance curves (Figure S3). In each force vs distance curve, the amplitude response and phase at two driving frequencies bounding the resonance frequency are monitored while the probe is moved into and out of the test fluid. These amplitude and phase values can then be used to estimate the amplitude vs frequency relationship of the resonance peak by using a damped harmonic oscillator model. The quality factor Q of the resonance peak is defined as the resonance frequency divided by the full width at half-maximum (FWHM) of the resonance peak and is inversely proportional to the damping force. A single DART curve can provide near continuous measurement of damping forces as a function of insertion depth L in a duration of <10 s. As seen in Figure S3c, the magnitude of Q^{-1} measured by DART increases linearly

with insertion depth beyond an initial region of <100 nm where surface forces may dominate.[9] Furthermore, when normalized by viscosity, these slopes dQ^{-1}/dL are within 15% between 202 and 600 mPa·s and within 33% between 202 and 4700 mPa·s despite large changes in Q. Therefore, at a given insertion length, the measured cantilever damping is a proxy for viscosity, especially for small changes, consistent with previous findings.[9,12]

Having characterized the cantilever response to liquids of known viscosities, we turned to the spatially restricted digital light processing (DLP) exposure of a photopolymer resin. To accomplish this, we employed a custom-built instrument (Figure S5), where a spatial light modulator (SLM) is used to selectively direct light from a 405 nm LED to the sample plane of an AFM.[14] This selective illumination from below can be used to create light patterns that are used in DLP and allows for in situ interrogation during photopolymerization. The test requires only a few microliters of resin, which could dramatically reduce the costs associated with novel resin formulation. We designed a resin based on the radical thiol–ene reaction, which proceeds effectively in the presence of oxygen due to the ability of thiols to reinitiate the polymerization following peroxy radical formation.[15] Although acrylate-based resins lead the commercial market, thiol–enes have been introduced in both linear and cross-linked formulations for additive manufacturing.[1,16,17] For the resin, a tetrafunctional thiol (pentaerythritol tetrakis(3-mercaptopropionate), PETMP) and a difunctional alkene (tri(ethylene glycol) divinyl ether, TEGDVE) were mixed together with an excess of alkene functionalities (0.64 thiol:1 alkene) to delay the gel point and increase the observable window of conversions. The photoinitiator diphenyl(2,4,6-trimethylbenzoyl)phosphine oxide (TPO) was included at 1 wt % due to its moderate absorption (≈200 L mol^{-1} cm^{-1}) at wavelength λ = 405 nm,[18] leading to an absorbance through 5 μm of resin of less than 0.01 (Figure S6). In addition, the numerical aperture (NA) of the microscope objective is low enough (0.4) that the beam can be approximated to have a profile that is uniform in the axial dimension, given the axial Rayleigh criterion 2λ/NA^2 of 5.0 μm. This, in combination with the low light attenuation and lack of oxygen inhibition, yields a reaction profile that can be assumed uniform in the axial dimension, which suits the uniform axial profile of the cylindrical probe.

We first desired to test whether photoinitiated liquid polymerization would be detectable through changes in viscosity. The molecular weight of step-growth polymers such as thiol–ene networks increases gradually at low conversions, before rapidly increasing near the gel point;[19] therefore the associated changes in viscosity at low conversion are expected to be modest, and non-Newtonian contributions have been neglected. Low conversion also prevents gelation and damage to the probe. Although nanocylinder-based viscosity metrology has been shown to be an accurate method for a range of static fluids, it was unknown whether it would be sensitive enough to detect changes associated with a small increase in molecular weight, particularly for spatially localized changes, as in DLP. With the nanocylinder inserted a known length (L = 2 μm) into the resin, 405 nm light was directed onto the sample. This resulted in an immediate increase in the damping coefficient ζ = 1/(2Q) (Figure 1c). As expected, higher light intensities led to more rapid increases in damping measured by the probe due to increased radical generation
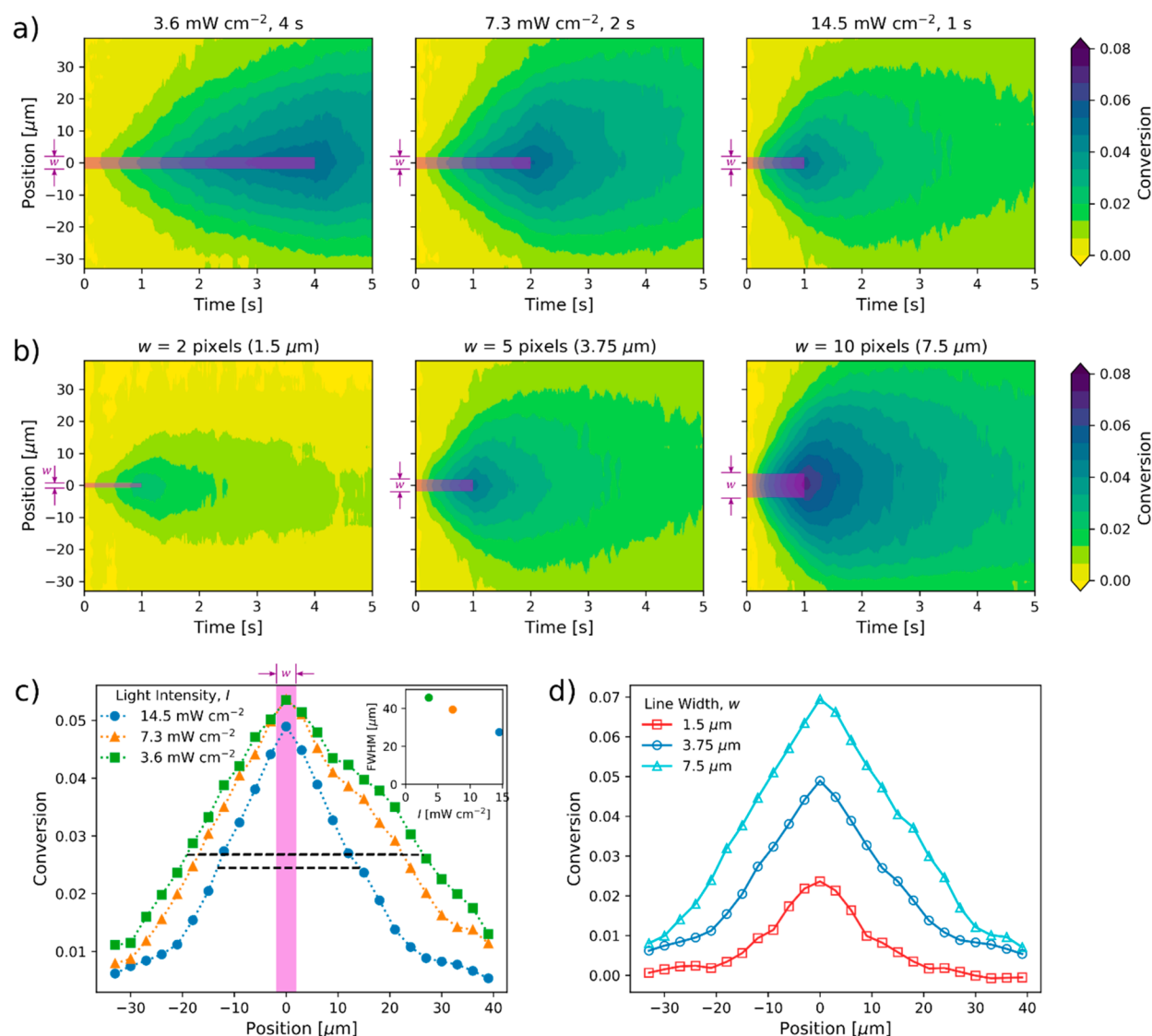
Figure 2. By relating the SCRPR damping ratio to viscosity and then conversion, spatial maps of conversion vs time for different exposure conditions can be measured. Higher viscosity species are generated in—and diffuse away from—the illuminated regions. The rectangular shaded regions indicate the spatial extent and duration of the light exposure. The plot color indicates the conversion. (a) Effect of light intensity on the spatial conversion profile. Light intensities of 3.6 mW cm^{-2} (left), 7.3 mW cm^{-2} (center), and 14.5 mW cm^{-2} (right) were used, and the exposure time was adjusted to maintain a constant dose of 14.5 mJ cm^{-2}. Higher light intensities led to sharper gradients but lower overall conversion. (b) Effect of SLM feature size on the viscosity profile. Increasing feature width led to higher conversion at a given light intensity and duration. (c) Profiles from (a) at the end of light exposure (4, 2, or 1 s) show higher conversion and more diffusion of polymer for low-dose, longer exposure time. Inset: full width at half-maximum (FWHM) of the conversion profiles at the different light intensities. (d) Profiles from (b) at 1 s show a marked increase in conversion for the larger illuminated area due to the cooperativity of adjacent voxels in generating polymeric species.

rate. However, if we examine the effect of light intensity I by examining the total dose $E = I \times t_{exp}$, we see that the lower light intensities led to increased total amount of damping after the equivalent $E = 14.5$ mJ cm^{-2} dose. This result may be explained by the fact that bimolecular termination (the classical termination reaction in radical polymerizations) increases with the square of radical concentration. In practice, thiol−ene photopolymerizations have been found to terminate with a combination of bi- and unimolecular reactions, leading to power law reaction rate dependencies on light intensity between 0.56 and 0.94.[20] Values of this exponent below unity led to smaller kinetic chain lengths at higher initiation rates. Therefore, although the polymeric species are generated more slowly and have more time to diffuse away from the illuminated region, the increased efficiency of the low light

intensity reaction outweighs this effect. While not observed with the light intensities herein, there no doubt exists a limit to this effect at low light intensity when the reaction time scale becomes long relative to the diffusion time.

Having shown that localized kinetic measurements of polymerization are possible, we next sought to obtain a one-dimensional reaction rate profile of a polymerizing voxel. To accomplish this, we directed a thin rectangle (112.5 μm × 1.5 μm) of light onto the resin and tracked the change in damping of the oscillating probe (Figure 1b). To map the reaction rate profile, the illuminated line was translated a distance d relative to the tip by using the spatial light modulator before subsequent light exposure. As d increases, the accumulation of polymer is delayed (Figure 1d). By limiting the light dose to maintain the resin in the liquid state, the measurement is
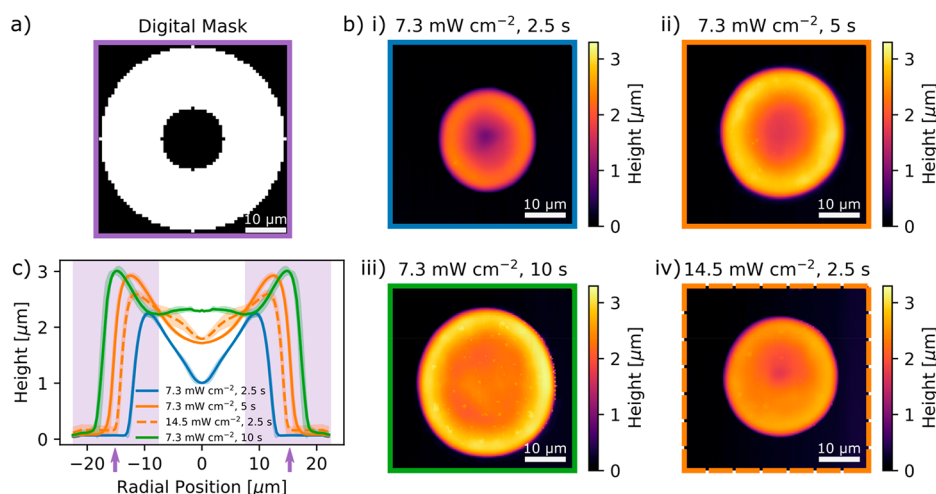
Figure 3. Diffusion effects on the photopolymerization of an enclosed ring test structure. (a) The digital mask projected onto the samples from the spatial light modulator. (b) AFM height profiles of structures created by 405 nm light exposure for 2.5 s (i), 5 s (ii), and 10 s (iii) at 7.3 mW cm^{-2} and 2.5 s at 14.5 mW cm^{-2} (iv). Panels ii and iv correspond to equivalent light doses (10 mJ cm^{-2}) but show different profiles. Scale bars 10 μm. (c) Radially averaged height profiles of the four structures with regions of light illumination indicated by violet shading. Unintended polymerization is observed in the ring center even at 2.5 s and occurs before the outer regions of the illuminated zone reach gelation. In this test, a higher light intensity (4 mW cm^{-2}, orange dashed line) leads to decreased fidelity to the pattern, with increased overpolymerization in the center and decreased polymerization toward the outer edges compared to 2 mW cm^{-2} (orange solid line) at equal dose. Lines and shaded regions correspond to the radial mean $\pm$ standard deviation.

effectively reversible (as confirmed by repeated measurements of the same exposure; Figure S7), as the pregelation polymer generated in the small reaction volume ($\approx$0.5 pL) diffuses into the surrounding resin (10 μL) in ~1 min (Figure 1d). Thus, the tip remains stationary as the region to be illuminated is shifted, and successive exposures can be performed to map the generation and diffusion of polymeric species.

To calculate the relationship between conversion p and viscosity for the thiol−ene resin, we used a custom-built rheo-Raman microscope that allows simultaneous *in situ* Raman measurements during photorheological traces, yielding a direct correlation between resin viscosity and conversion (Figure S8).[21] With a quantitative relationship between viscosity and conversion, we can spatially map conversion during photopolymerization using the AFM. We were specifically interested in the effects of light intensity and illuminated feature size on the spatial distribution of polymeric species. To assess these effects, we first studied the effect of changing light intensity (3.6, 7.3, and 14.5 mW cm^{-2}) at a constant dose of 14.5 mJ cm^{-2} and a constant feature size w of 3.75 μm, corresponding to 5 pixels of the SLM. To approximate a one-dimensional profile, the lateral dimension of the digital mask was set to 112.5 μm (150 pixels). As seen in Figure 2a, the higher light intensity photopolymerizations led to higher rates and slightly sharper gradients in the conversion profile. However, as before in Figure 1c, the final conversion is lower for the higher intensities, again likely due to increased radical termination at higher initiating rates, which outweighs the increased time for diffusion. Consequently, despite a 4-fold increase in light intensity, only a 40% decrease in the full width at half-maximum (FWHM) of the conversion profile is measured (Figure 2c, inset). If we compare the reactions at equal maximum conversions of $p = 0.04$, similar improvement is observed (39%, Figure S9). These results emphasize the diminishing returns of increasing light intensity in non-reciprocal photopolymerizations. Other strategies currently in use such as increasing the resin viscosity to decrease the mass

transport rate or increasing the number of functional groups on monomer species to lower the gel point might be more effective at increasing the print resolution. Of course, high-viscosity resins also need to contend with increased separation forces from the print window,[22] and low gel points can cause greater polymerization-induced stress and part deformation.[1] Another observation from our measurements is that for line positions other than directly under the probe the maximum conversion is experienced after the light is shuttered—by up to 2 s—due to the time required for the polymers generated at the light source to diffuse to the probe. Conversion profiles continue to evolve even after the light is shuttered, which may affect the reaction in subsequent layers. We next evaluated the effect of illuminated feature size at constant light intensity (14.5 mW cm^{-2}), shown in Figure 2b. Although the light intensity at each pixel is kept constant, we observe the cooperative effect of adjacent pixels in increasing the local extent of reaction. This leads to a pronounced difference in the conversion profiles at the end of the exposure (Figure 2d) and demonstrates that strategies such as grayscale correction[23] likely need to be imposed to obtain uniform cure and resolution in a layer with features of different sizes. One consequence predicted by this diffusion profile is that spatial variability in gel time and mechanics will arise within layers of SLA parts due to the proximity of neighboring illuminated voxels. This extends beyond adjacent voxels to include any that lie within the diffusion length of the resin in the time scale of a layer cure. A higher local density of illuminated voxels will correspond to an increased local buildup of polymeric species. Furthermore, there are geometric implications as well because enclosed shapes are better able to accumulate reacted monomer. Thus, it is expected that these regions will reach the gel point faster, reach higher conversions at the same light dose, and ultimately end up more highly cross-linked. To illustrate this effect, we photopolymerized a test structure in the shape of an enclosed ring with dimensions (inner diameter = 15 μm, outer diameter = 45 μm) chosen to match the length

scales of the gradients from Figures 1 and 2, i.e., tens of micrometers, and quantified the topography of the resulting features with AFM (Figure 3). Notably, substantial polymerization was detected in the dark center of the ring even at the lowest light exposure setting (7.3 mW cm^{-2}, 2.5 s) and occurred well before the outer edges of the illuminated region (Figure 3c, shaded) reached the gel point conversion. Despite the lack of photoinitiation in this region, reacted species accumulate to such a degree that incidental initiation (likely via light scattering) leads to rapid gelation and a loss of print resolution. Significant initiation is not anticipated due to the imperfect dark level of the SLM (nominal contrast ratio = 200:1) because when the same digital mask was used to stiffen a dual-cure film, good fidelity to the mask was observed (Figure S10). Height variation is likely due to differences in gel fraction before the wash step, and raised edges characteristic of DLP[24] can also be seen. We again evaluated the effect of light intensity by printing two structures with equivalent light doses of 36 mJ cm^{-2} but varied the light intensity from 7.3 mW cm^{-2} to 14.5 mW cm^{-2}, as seen in Figure 3b(ii,iv). Interestingly, the higher light dose resulted not only in less gelation in the outer region of the illuminated ring but relatively more polymerization in the ring center. Consequently, the overall height profile of the structure is flatter than the lower-intensity counterpart and less true to the digital mask. Thus, the lack of exposure reciprocity observed in kinetic measurements translates to altered resolution in practice.

Like epoxide resins, the thiol—ene resin in this study is less sensitive to the effects of oxygen than acrylate-based formulations. While the effect of oxygen depletion within the reaction volume is not captured here, it may be important for other resins. Delrot and co-workers examined the effect of light intensity on triacrylate photopolymerization for focused laser spots, finding lower light intensities required a higher total dose due to the inability to sufficiently deplete oxygen in the small reaction volume.[25] This contrasts with uniform curing of multiacrylates, which display sublinear light dependencies (power law relationships as small as $I^{0.3}$).[6] We therefore propose that to predict the light dose or intensity dependence of a photopolymerization reaction, all of the following factors should be taken into account: (1) the diffusion rates of reactive species and (if applicable) oxygen, (2) the reaction rate and gel point, and (3) the size and shape of the polymerized region. Although the concept of a critical energy dose E_c has been applied with wide success in the past,[4,26] this context will be essential for the design of evenly cured high resolution parts. Our future efforts will apply this SCRPR technique to study voxel interactions in the sample plane to address this gap. The inclusion of absorbers is also necessary in SLA to restrict light to the working layer, creating light gradients in the print direction. We hypothesize that our technique would be valid for submerged probes[27] to allow us to fully map the three-dimensional conversion profile *in situ* during a stereolithographic printing step.

CONCLUSION

In summary, we have demonstrated a method for measuring local reaction rates in the vicinity of a photopolymerizing region of resin using only a few microliters of resin. Resonance damping of an oscillating nanocylinder is related to local monomer conversion through the viscosity of the resin. Measurements of the conversion profiles in a thiol—ene resin show polymer accumulation tens of micrometers away from

the light source during brief (1−4 s) exposures, highlighting the role of diffusion in stereolithography. The spatial distribution of polymerization is found to depend strongly on exposure conditions, invalidating the assumption that conversion depends only on energy dose. Furthermore, increased intensity and decreased duration of exposure do not appreciably confine the reaction volume and diminish the overall conversion, indicating other processing pathways to enhanced resolution are necessary. Ring structures printed with feature sizes matching the diffusion length show rapid overpolymerization in the enclosed region due to the buildup of reacted species. Physical estimates and finite volume modeling indicate that the measurement volume is localized to within ∼1 μm of the probe, which gives sufficient resolution for current stereolithographic techniques with pixels in the tens of micrometers and the ∼20 μm concentration gradient length scales measured in this work. The possibility to operate at higher frequencies by changing cantilevers or choosing higher eigenmodes should push the resolution still higher.

METHODS

Computational Fluid Dynamics (CFD) Modeling. A fluid dynamics simulation using the finite volume method was constructed by using Ansys Fluent software. The probe radius is set to 60 nm with a hemispherical end-cap. The two-phase model (liquid and air) is solved for both the mass conservation and momentum balance for each phase as well as the surface tension for the fluids in contact with the cylindrical probe. For the surface tension, the conservative continuum surface stress approach is used, and a premodel step is included to allow the meniscus to rise to an equilibrium position h_{men} of 220 nm. Liquid viscosities of 202, 600, and 4700 mPa·s were chosen to match the viscosities of the test fluids for the AFM verification. The oscillation amplitude was set to 5 nm, and frequencies of 50 and 300 kHz were used to approximate the first and second free resonance frequencies of the AFM cantilevers. Nominal insertion lengths L' of 600 and 1200 nm were studied for each liquid.

AFM Viscosity Measurements. Viscosity standards were measured by using AFM cantilevers with Ag$_2$Ga nanowires extending from the tips (NN-HAR-FM60, NaugaNeedles, USA), with nominal tip radius of curvature of 50 nm, 60 kHz first free resonance frequency, and spring constant of 3 N m^{-1}. Cantilevers were imaged with scanning electron microscopy prior to use to measure cylinder geometry. Spring constants were determined from thermal spectra for all probes.[28] Measurements were performed on an Asylum Cypher microscope by using photothermal cantilever actuation during triggered force curves in dual AC resonance tracking (DART) mode.[13] The amplitude and phase response at two forcing frequencies bounding the resonance frequency are used to reconstruct the resonance quality factor Q. Force vs distance curves were used to move the cylindrical probe into and out of a thin layer of liquid while tracking Q. Damping was determined by using Q during retraction of the probe. The separation point of the probe from the liquid surface was treated as the zero point for insertion length. The capillary force (F_{cap}) is determined from the difference in cantilever deflection as the probe releases from the liquid. A small increase in capillary force corresponds to the changing contact angle as the probe exits the liquid; the difference in height between this point and the free surface (measured during probe extension) was estimated as the meniscus height ($\approx h_{men}$).

Drag Force Estimates. Viscous drag forces for SCRPR experiments were calculated from the measured quality factor Q and cantilever stiffness k:

$$F_{d,max} = \frac{k}{Q}A$$

The quality factor was found to be independent of amplitude (Figure S4), so the drag force was corrected to $A = 5$ nm amplitude to match the CFD simulations, given Q at any A. The cantilever stiffness for the second eigenmode was assumed to be 40.2 times the measured stiffness of the first eigenmode.[29] The CFD simulation directly outputs the total drag force. For comparison, two additional estimates of drag force were performed. In the first, adapting the Broersma method for a cylinder under flow,[11] the drag force F_d can be calculated as

$$F_d = \frac{2\pi\eta Lu}{\ln\left(\frac{2L}{R}\right) - 0.81}$$

with viscosity η, length L, radius R, and velocity u in the axial direction. Drag forces were calculated by assuming an insertion length $L = L' + h_{men}$. For the oscillatory motion $A \times \cos(2\pi ft - \phi)$ of the cantilever, the maximum drag force occurs at the peak velocity $v_0 = 2\pi fA$ with amplitude A, frequency f, time t, and phase lag ϕ. Second, the drag force was calculated from the Stokes solution for an oscillating cylinder given by De Baubigny et al.[12]

$$F_d = 2\pi rL\frac{\eta}{\delta}(1-i)\frac{K_1\left[(1-i)\frac{R}{\delta}\right]}{K_0\left[(1-i)\frac{R}{\delta}\right]}e^{-i2\pi ft}$$

where $\delta = \sqrt{\frac{\eta}{\rho\pi f}}$ is the viscous layer thickness for the two-dimensional case (i.e., an oscillating wall), and K_1 and K_0 are modified Bessel functions of the second kind. The drag force oscillates within an envelope, which, for $R/\delta \ll 1$, simplifies to[12]

$$F_{d,max} = 2\pi L\eta v_0\frac{-1}{\ln\left(\frac{R}{\delta}\right)}$$

AFM/SLA Photorheology and Photopolymerization. To perform *in situ* measurements of the photopolymerization reaction, a custom-built instrument[14] that enables simultaneous light patterning and AFM measurements was used (Figure S5). Briefly, 405 nm light (M405LP1, Thorlabs) is projected to the sample plane of an inverted optical microscope (Olympus PLN) via the side port. Photopattern formation is achieved with a spatial light modulator (E-Series, Meadowlark Optics). A Molecular Force Probe 3D (Asylum Research) AFM is positioned on the optical microscope such that the AFM probe lies in the photopatterning region. The thiol−ene resin was composed of 50 μL of PETMP (64.5 mg) and 30 μL of TEGDVE (30 mg), with a final photoinitiator (TPO) concentration of 1 wt %. Ten microliters of resin was spread in a thin layer ($\approx$5 μm) across a glass slide. With the probe inserted into the resin, a triggered force curve was initiated with DART tracking engaged during the forward dwell. A defined voltage pattern was used to drive the LED from the AFM software. To approximate a one-dimensional exposure profile, a single line of 150 pixels (112.5 μm) in length and varying width was used as the photopattern. A period of 60 s between successive light exposures was used to allow the partially reacted resin to equilibrate with the surroundings (see Figure 2C). To create spatial maps of the reaction, the illuminated line was shifted relative to the probe by using the SLM. Because of the imperfect dark level of the spatial light modulator (200:1 contrast ratio), a baseline increase was observed during irradiation without illuminated pixels, and this baseline was subtracted from each polymerization condition. A similar method was used for photopolymerization of the ring-shaped test structures in Figure 3. The projected pattern was changed to the digital mask in Figure 3a, and the larger illuminated area and longer exposure time brought the resin above the gel point in select regions. The test structures adhered to the glass window and were washed by gently pipetting 50 μL of acetone and then returned to the instrument for force−volume mapping.

Rheo-Raman Spectroscopy. A rotational rheometer (Thermo-Scientific HAAKE MARS III) modified to allow Raman spectroscopy (Thermo Scientific DXR) through a transparent base was used.[21] The rheometer was operated in a parallel plate geometry (gap height 0.3 mm, diameter 20 mm) with a clear upper plate to allow light illumination via a mercury vapor lamp (Excelitas Omnicure S2000). The lamp was operated with an external 400−500 nm bandpass filter, and the light intensity at the sample was 21 mW cm^{-2}. With an additional bandpass filter (400 $\pm$ 20 nm, Thorlabs) in place, the light intensity was 5 mW cm^{-2}, giving the intensity of the 405 nm emission band and thus the effective light intensity due to the dropoff in absorption of the photoinitiator TPO above this range.[18] Steady-shear viscosity measurements were performed between successive light exposures, and Raman spectra were acquired continuously. A 780 nm laser with a power of 24 mW was used. Each recorded spectrum had a total collection time of 20 s and consisted of four exposures of 5 s duration. The thiol concentration was monitored as the S−H stretch (2574 cm^{-1}) peak area, with the carbonyl C═O stretch (1743 cm^{-1}) as an internal standard. The shear viscosity diverges to infinity at the gel point ($p = p_{gel}$), and the viscosity (η) was fit to[19]

$$\eta = \eta_0\left(1 - \frac{p}{p_{gel}}\right)^{-\alpha}$$

where α and p_{gel} are adjustable parameters and η_0 is the starting viscosity (21 mPa·s). Two independent trials were performed, and the data were fit in aggregate, yielding $p_{gel} = 0.79 \pm 0.02$ and $\alpha = 1.20 \pm 0.09$. This agrees well with the theoretical gel point of 0.72 (eq S7), considering a small delay as the result of cyclization (i.e., loop formation).[30]

Dual Cure Film Stiffening. PETMP (65 mg, 0.13 mmol), TMPTA (17.4 mg, 0.59 mmol), TEGDVE (36 mg, 0.18 mmol), and TPO (0.7 mg, 0.6 wt % final) were mixed, and 1 mg of N',N',N',N'-tetramethylethylenediamine was added to catalyze the first stage of the reaction. The resulting liquid was cast between a glass coverslip and a 22 mm × 22 mm section of Teflon film to create a film of $\approx$5 μm thickness. The first stage of the reaction, nucleophilic thiol−ene reaction between the thiol of PETMP and the acrylate of TMPTA, was allowed to proceed in the dark for 2 h before the Teflon was removed and the sample was placed in the hybrid SLA/AFM. The second stage of the reaction is the photoinitiated radical thiol−ene reaction between TEGDVE and the remaining thiols. The ring-shaped test pattern (inner diameter = 15 μm, outer diameter = 45 μm) was directed onto the sample (405 nm, 4 mW cm^{-2}, 2.5 s), and then the region was analyzed by force−volume mapping. To determine the sample elastic modulus, the force vs distance curves were fit by using the Johnson−Kendall−Roberts (JKR) contact mechanics model, and the AFM tip shape was measured by scanning electron microscopy.

Data Analysis. The analysis and scientific workflow were performed in the Python programming language and are available as Jupyter notebooks at https://github.com/tbrow/AFM_photorheology.

■ ASSOCIATED CONTENT

Ⓢ **Supporting Information**
The Supporting Information is available free of charge at https://pubs.acs.org/doi/10.1021/acsapm.0c01090.

Figures S1−S10, Tables S1 and S2 (PDF)

■ AUTHOR INFORMATION

Corresponding Author
  Jason P. Killgore − *Applied Chemicals and Materials Division, National Institute of Standards and Technology, Boulder, Colorado 80305, United States*; Email: jason.killgore@nist.gov

Authors
  Tobin E. Brown − *Applied Chemicals and Materials Division, National Institute of Standards and Technology, Boulder, Colorado 80305, United States*; Ⓞ orcid.org/0000-0002-7852-7561

Veruska Malavé — *Applied Chemicals and Materials Division, National Institute of Standards and Technology, Boulder, Colorado 80305, United States*

Callie I. Higgins — *Applied Chemicals and Materials Division, National Institute of Standards and Technology, Boulder, Colorado 80305, United States;* ⊙ orcid.org/0000-0002-0649-158X

Anthony P. Kotula — *Materials Science and Engineering Division, National Institute of Standards and Technology, Gaithersburg, Maryland 20899, United States;* ⊙ orcid.org/0000-0002-0830-2869

Benjamin W. Caplins — *Applied Chemicals and Materials Division, National Institute of Standards and Technology, Boulder, Colorado 80305, United States*

Edward J. Garboczi — *Applied Chemicals and Materials Division, National Institute of Standards and Technology, Boulder, Colorado 80305, United States*

Complete contact information is available at:
https://pubs.acs.org/10.1021/acsapm.0c01090

Author Contributions

T.E.B. and V.M. contributed equally to this work.

Notes

The authors declare no competing financial interest.

■ REFERENCES

(1) Ligon, S. C.; Liska, R.; Stampfl, J.; Gurr, M.; Mülhaupt, R. Polymers for 3D Printing and Customized Additive Manufacturing. *Chem. Rev.* **2017**, *117* (15), 10212−10290.

(2) Odian, G. *Principles of Polymerization*; John Wiley & Sons, Inc.: Hoboken, NJ, 2004.

(3) Stampfl, J.; Baudis, S.; Heller, C.; Liska, R.; Neumeister, A.; Kling, R.; Ostendorf, A.; Spitzbart, M. Photopolymers with Tunable Mechanical Properties Processed by Laser-Based High-Resolution Stereolithography. *J. Micromech. Microeng.* **2008**, *18* (12), 125014.

(4) Jacobs, P. F. Rapid Prototyping & Manufacturing—Fundamentals of Stereolithography. *J. Manuf. Syst.* **1993**, *12* (5), 430−433.

(5) Zhu, W.; Ma, X.; Gou, M.; Mei, D.; Zhang, K.; Chen, S. 3D Printing of Functional Biomaterials for Tissue Engineering. *Curr. Opin. Biotechnol.* **2016**, *40*, 103−112.

(6) Bowman, C. N.; Kloxin, C. J. Toward an Enhanced Understanding and Implementation of Photopolymerization Reactions. *AIChE J.* **2008**, *54* (11), 2775−2795.

(7) Odian, G. *Principles of Polymerization*, 4th ed.; Wiley & Sons: New York, 2004.

(8) Fiedler-Higgins, C. I.; Cox, L. M.; DelRio, F. W.; Killgore, J. P. Monitoring Fast, Voxel-Scale Cure Kinetics via Sample-Coupled-Resonance Photorheology. *Small Methods* **2019**, *3* (2), 1800275.

(9) Yazdanpanah, M. M.; Hosseini, M.; Pabba, S.; Berry, S. M.; Dobrokhotov, V. V.; Safir, A.; Keynton, R. S.; Cohn, R. W. Micro-Wilhelmy and Related Liquid Property Measurements Using Constant-Diameter Nanoneedle-Tipped Atomic Force Microscope Probes. *Langmuir* **2008**, *24* (23), 13753−13764.

(10) Broersma, S. Viscous Force Constant for a Closed Cylinder. *J. Chem. Phys.* **1960**, *32* (6), 1632−1635.

(11) Cox, R. G. The Motion of Long Slender Bodies in a Viscous Fluid. Part 1. General Theory. *J. Fluid Mech.* **1970**, *44* (04), 791.

(12) Dupré de Baubigny, J.; Benzaquen, M.; Mortagne, C.; Devailly, C.; Kosgodagan Acharige, S.; Laurent, J.; Steinberger, A.; Salvetat, J. P.; Aimé, J. P.; Ondarçuhu, T. AFM Study of Hydrodynamics in Boundary Layers around Micro- and Nanofibers. *Phys. Rev. Fluids* **2016**, *1* (4), 1−18.

(13) Gannepalli, A.; Yablon, D. G.; Tsou, A. H.; Proksch, R. Mapping Nanoscale Elasticity and Dissipation Using Dual Frequency Contact Resonance AFM. *Nanotechnology* **2011**, *22* (35), 355705.

(14) Higgins, C. I.; Brown, T. E.; Killgore, J. P. Digital Light Processing in a Hybrid Atomic Force Microscope: In situ, Nanoscale Characterization of the Printing Process. *Additive Manufacturing* Accepted Dec. 2020.

(15) Hoyle, C. E.; Lee, T. Y.; Roper, T. Thiol-Enes: Chemistry of the Past with Promise for the Future. *J. Polym. Sci., Part A: Polym. Chem.* **2004**, *42* (21), 5301−5338.

(16) Wallin, T. J.; Pikul, J. H.; Bodkhe, S.; Peele, B. N.; Mac Murray, B. C.; Therriault, D.; McEnerney, B. W.; Dillon, R. P.; Giannelis, E. P.; Shepherd, R. F. Click Chemistry Stereolithography for Soft Robots That Self-Heal. *J. Mater. Chem. B* **2017**, *5* (31), 6249−6255.

(17) Alim, M. D.; Childress, K. K.; Baugh, N. J.; Martinez, A. M.; Davenport, A.; Fairbanks, B. D.; McBride, M. K.; Worrell, B. T.; Stansbury, J. W.; McLeod, R. R.; Bowman, C. N. A Photopolymerizable Thermoplastic with Tunable Mechanical Performance. *Mater. Horiz.* **2020**, *7* (3), 835−842.

(18) Leprince, J. G.; Hadis, M.; Shortall, A. C.; Ferracane, J. L.; Devaux, J.; Leloup, G.; Palin, W. M. Photoinitiator Type and Applicability of Exposure Reciprocity Law in Filled and Unfilled Photoactive Resins. *Dent. Mater.* **2011**, *27* (2), 157−164.

(19) Larson, R. G. *The Structure and Rheology of Complex Fluids*, 1st ed.; Oxford University Press: New York, 1999.

(20) Scott, T. F.; Kloxin, C. J.; Draughon, R. B.; Bowman, C. N. Nonclassical Dependence of Polymerization Rate on Initiation Rate Observed in Thiol-Ene Photopolymerizations. *Macromolecules* **2008**, *41* (9), 2987−2989.

(21) Kotula, A. P.; Meyer, M. W.; De Vito, F.; Plog, J.; Hight Walker, A. R.; Migler, K. B. The Rheo-Raman Microscope: Simultaneous Chemical, Conformational, Mechanical, and Microstructural Measures of Soft Materials. *Rev. Sci. Instrum.* **2016**, *87* (10), 105105.

(22) Pan, Y.; He, H.; Xu, J.; Feinerman, A. Study of Separation Force in Constrained Surface Projection Stereolithography. *Rapid Prototyp. J.* **2017**, *23* (2), 353−361.

(23) Peterson, G. I.; Schwartz, J. J.; Zhang, D.; Weiss, B. M.; Ganter, M. A.; Storti, D. W.; Boydston, A. J. Production of Materials with Spatially-Controlled Cross-Link Density via Vat Photopolymerization. *ACS Appl. Mater. Interfaces* **2016**, *8* (42), 29037−29043.

(24) Higgins, C. I.; Killgore, J. P.; DelRio, F. W.; Bryant, S. J.; McLeod, R. R. Photo-Tunable Hydrogel Mechanical Heterogeneity Informed by Predictive Transport Kinetics Model. *Soft Matter* **2020**, *16*, 4131.

(25) Delrot, P.; Loterie, D.; Psaltis, D.; Moser, C. Single-Photon Three-Dimensional Microfabrication through a Multimode Optical Fiber. *Opt. Express* **2018**, *26* (2), 1766.

(26) Tumbleston, J. R.; Shirvanyants, D.; Ermoshkin, N.; Janusziewicz, R.; Johnson, A. R.; Kelly, D.; Chen, K.; Pinschmidt, R.; Rolland, J. P.; Ermoshkin, A.; Samulski, E. T.; DeSimone, J. M. Continuous Liquid Interface Production of 3D Objects. *Science (Washington, DC, U. S.)* **2015**, *347* (6228), 1349−1352.

(27) Ziegler, D.; Klaassen, A.; Bahri, D.; Chmielewski, D.; Nievergelt, A.; Mugele, F.; Sader, J. E.; Ashby, P. D. Encased Cantilevers for Low-Noise Force and Mass Sensing in Liquids. *2014 IEEE 27th Int. Conf. Micro Electro Mech. Syst.* **2014**, 128−131.

(28) Hutter, J. L.; Bechhoefer, J. Calibration of Atomic-Force Microscope Tips. *Rev. Sci. Instrum.* **1993**, *64* (7), 1868−1873.

(29) Melcher, J.; Hu, S.; Raman, A. Equivalent Point-Mass Models of Continuous Atomic Force Microscope Probes. *Appl. Phys. Lett.* **2007**, *91* (5), 1−4.

(30) Valles, E. M.; Macosko, C. W. Structure and Viscosity of Poly(Dimethylsiloxanes) with Random Branches. *Macromolecules* **1979**, *12* (3), 521−526.